Collapse of a composite beam made from ultra high molecular-weight polyethylene fibres

G Liu*, M D Thouless, V S Deshpande* and N A Fleck***

* Cambridge University Engineering Dept., Trumpington St., Cambridge, CB2 1PZ, UK

** Dept. of Mechanical Engineering, and Dept. of Materials Science & Engineering, University of Michigan, Ann Arbor, MI 48109-2125, USA

15 August 2013

Abstract

Hot-pressed laminates with a $[0/90]_{48}$ lay-up, consisting of 83% by volume of ultra high molecular-weight polyethylene (UHMWPE) fibres, and 17% by volume of polyurethane (PU) matrix, were cut into cantilever beams and subjected to transverse end-loading. The collapse mechanisms were observed both visually and by X-ray scans. Short beams deform elastically and collapse plastically in longitudinal shear, with a shear strength comparable to that observed in double notch, interlaminar shear tests. In contrast, long cantilever beams deform in bending and collapse via a plastic hinge at the built-in end of the beam. The plastic hinge is formed by two wedge-shaped microbuckle zones that grow in size and in intensity with increasing hinge rotation. This new mode of microbuckling under macroscopic bending involves both elastic bending and shearing of the plies, and plastic shear of the interface between each ply. The double-wedge pattern contrasts with the more usual parallel-sided plastic microbuckle that occurs in uniaxial compression. Finite element simulations and analytical models give additional insight into the dominant material and geometric parameters that dictate the collapse response of the UHMWPE composite beam in bending. Detailed comparisons between the observed and predicted collapse responses are used in order to construct a constitutive model for laminated UHMWPE composites.

1. Introduction

Ultra High Molecular-weight Polyethylene (UHMWPE) fibres in a polyurethane or polyethylene matrix have extremely high specific stiffness and strength, and are used in a wide range of applications from ropes to blast resistant armour. The fibres have been commercialised by DSM Dyneema® NL under the trade name Dyneema®. Commonly, Dyneema® laminated plates are hot pressed to a 0/90 cross-ply configuration. Materials tests on 0/90 UHMWPE composites have recently been reported by Russell et al. (2013), and by Iannucci and Pope (2011); these studies highlight the extreme anisotropic nature of the composite. For example, in uniaxial tension, the fibres dictate the tensile strength of the composite, and the tensile strength of the 0/90 laminate is about 800 MPa. In contrast, the in-plane shear strength of the 0/90 laminate is on the order of 1-2 MPa. However, surprisingly little is known about these laminates under simple loading states, such as bending. The purpose of the present study is to develop and make use of a cantilever bend test for Dyneema® laminated beams, and thereby to determine the constitutive parameters associated with beam bending.

The cantilever beam test contrasts with the more commonly used test methods of 3-point bending and 4-point bending as described in the following ASTM standards:

(i) ASTM Test Method D 2344/D 2344M-00 gives a protocol for short beam test to interrogate longitudinal shear properties; and

(ii) ASTM D7264 / D7264M – 07 gives a protocol for long beam tests to measure the bending strength.

Preliminary 3-point bend tests by the authors on Dyneema® beams indicate that the beams collapse in one of the two arms in an asymmetrical manner, and this complicates interpretation of the subsequent collapse response. To obviate this, a cantilever beam arrangement is employed in the present study.

There is a clear need to develop physically-based micromechanical models of deformation and failure for UHMWPE laminates, and to then use these models to obtain appropriate

material descriptions for finite element implementation. Such an approach requires direct observation of the physical collapse mechanisms for a range of stress states, from uniaxial straining, to bending, and to more complex, 3D stress states. The cantilever beam tests reported here are a first step in this direction.

The lack of materials data and of validated constitutive models for Dyneema® laminates has led to empirical approaches to modelling the performance of Dyneema®/UHMWPE laminates in practical applications. For example, the penetration resistance of UHMWPE composites for armour applications have concentrated on developing continuum damage-mechanics models (Utomo and Ernst (2008); Iannucci and Pope (2011); Iannucci and Willows (2006)) and softening-plasticity models (Grujicic et al. (2009)). These models are calibrated against projectile penetration data for both thin sheet and back-supported blocks, and are able to predict some of the observed penetration mechanisms such as delamination and inter-laminar shear. However, the dynamic penetration tests are too complex for the derivation of basic constitutive properties, and a set of *independent* simple structural tests are required to achieve this. The materials data accrued from idealised structural tests, such as the cantilever beam test, are an important first step in the measurement of relevant materials data for the construction of constitutive models.

The scope of this paper is as follows. The transverse elastic deflection and collapse response of end-loaded Dyneema® composite beams are measured as a function of beam length, and the associated collapse mechanisms are observed both visually and by X-ray scans. A detailed finite element model is then used to predict the collapse response.

2. Experimental investigation of UHMWPE composite cantilever beams

2.1 Geometry of UHMWPE composite cantilever beam

Hot-pressed Dyneema® laminate plates, of commercial designation HB26, were obtained from DSM. The laminates were of a $[0/90]_{48}$ lay-up, and consisted of 83% by volume of UHMWPE fibres, and 17% by volume of polyurethane (PU) matrix. The plates were of

dimensions 400x400x6 mm, and were taken from the same batch of material as that used by Russell et al. (2013) to measure the in-plane tensile properties and shear properties.

Beams of height h =6mm, length L =6mm to 300mm and width W=20mm were cut from the HB26 plates and one end of each beam was clamped between two thick steel plates of the test fixture, as sketched in Fig. 1. The free end of the beams was loaded via a steel cylinder of diameter d=6.4mm using a screw-driven testing machine. Unless otherwise stated, a cross-head speed of 2mm/min was employed in all tests. The overhang s between the end of the beam and the roller was 10mm. In preliminary tests, this overhang was increased to 20mm and the width of the beams was increased to 35mm; there was no observable effect of these changes in geometry on the response of the beam in terms of the load per unit width P versus roller displacement δ .

Two sets of beam tests were performed. In the first, the applied loads were kept sufficiently small for the beams to behave in an elastic manner, avoiding permanent deformation; these tests were used to extract the elastic properties. And, in a second set of tests, the beams were loaded to plastic collapse.

2.2 Elastic properties of the composite beams

For all beam lengths and loading rates, the initial portion of the P versus δ curve is linear. The measured unloading compliance $C = \delta/P$ is plotted as a function of beam length L in Fig. 2 for three applied loading rates. Typically, a specimen was subjected to a load of 10% peak load and then unloaded; the initial unloading slope was measured and used to define the elastic compliance of the specimen.

Two distinct regimes of deformation were observed, depending on the beam length. Short beams deformed in, shear, and the compliance being proportional to the beam length according to the approximate relationship (assuming the shear coefficient for the beam is unity):

$$C = \frac{\delta}{P} = \frac{L}{Gh} \qquad (1)$$

where G is the shear modulus of the beam. On fitting (1) to the measured response for beam lengths below 50mm, the slope of the compliance curve suggests that $G = 60 \pm 10$ MPa.

The response of the long beams, with L greater than about 100, was dominated by flexure, with the compliance is proportional to the cube of the beam length L, according to the usual beam formula

$$C = \frac{\delta}{P} = \frac{4L^3}{Eh^3} \qquad (2)$$

where E is the axial modulus of the beam. The constant of proportionality for the compliance curve suggests that E = 34 GPa. Note the large contrast in axial and shear moduli of the HB26 laminate: the axial modulus exceeds the shear modulus by three orders of magnitude. This can be traced to the highly drawn nature of the Dyneema® fibres. Consequently, a beam of short or moderate length (up to 5 times the beam height) deforms predominantly in shear. The transverse modulus of a unidirectional layer of the HB26 composite is also several orders of magnitude less than the axial modulus; upon making use of this assumption, the above bending tests on a $[0/90]_{48}$ beam suggest that the axial modulus of a unidirectional layer is 68 GPa.

It is instructive to compare the above values for axial and shear moduli with the recent measurements by Russell et al (2012). The axial modulus of a $0/90^o$ laminate is 25-50 GPa for strain rates in the range of 10^{-4} – 10^{-2} s^{-1} (by direct measurement of the loading slope of the data shown in Fig. 5a of Russell et al (2012)); the present value of 34 GPa lies within this range. Russell et al (2012) measured the in-plane shear modulus of HB26 composite via tension tests on a $\pm 45^o$ lay-up, see Fig. 5b of their paper. They found that the shear response is rate sensitive due to visco-elastic effects and, at a strain rate of 10^{-4} s^{-1}, the measured in-plane shear modulus is 60 MPa, in good agreement with the present measurements of 60 ± 10 MPa. Note that we do not expect exact agreement as the shear directions are different in the two studies: the beam tests of the present study give the longitudinal shear modulus whereas the tests reported by Russell et al (2012) give the in-plane shear modulus.

2.3 Plastic collapse of composite beams

A second set of clamped HB26 composite beam tests was conducted with the beams loaded monotonically to collapse. Typical load versus displacement responses are given in Fig. 3 for a short beam (L=10mm) and a long beam (L=100mm). In both cases, the initial response was followed by a peak load, hereafter referred to as the 'plastic collapse load'. Strong softening followed the peak load for the short beam tests while only a small load drop accompanied continued plastic collapse for the long beams.

The localised nature of the deformation accompanying the post-peak response was probed using optical microscopy and 3D X-ray tomography (C-scan machine, operating at 45kV). These images are included in Fig. 3, and reveal that the short beam collapsed by longitudinal shear along several interlaminar planes whereas the long beam collapsed by the formation of a plastic hinge. The hinge was located at the root of the beam, or in some cases 1-2mm from the root.

Additional insight into these two collapse mechanisms is gained by plotting the plastic collapse load per unit width P_{max} against beam length L in Fig. 4. For short beams, the collapse load was almost independent of beam length. Our interpretation is as follows. Assume that the beam behaves as a linear-elastic Timoshenko beam up to peak load, such that the shear stress at mid-plane is given by $\tau = 3P/(2h)$. A peak load per unit width of 12 N/mm and a beam height of h =6 mm implies an interlaminar shear strength of 3.0 MPa. In contrast, long beams collapse at a constant end moment, with the collapse load scaling inversely with beam length. The collapse moment/unit width for the longer beams is calculated from the slope of the load against beam length plot, and equals 200±40 N.

The plastic hinge at the root of the long beams was in the form of a kink-band, as sketched in Fig. 5a. An optical image of the kink band for a representative beam of length L = 100 mm is shown in Fig. 5b. In this image the black lines are markings that were initially parallel and placed on the side of the beam by a marker pen approximately 1 mm apart to aid visualisation of the collapse mechanism. Fig. 5c-d are scanning-electron microscope (SEM) images of the kink band at two different magnifications. It is clear from these images that the plastic hinge gives rise to rotation of the cross-section, while the images at higher magnification reveal two wedge-shaped kink zones as sketched in Fig. 5a. At any instant, the rotation of the plies within each zone is uniform, but as the hinge rotation increases, the hinge broadens and the degree of ply rotation increases within each zone. We parameterise the hinge size by the angle β subtended at the apex of the wedge as sketched in Fig. 6a: the measured β is plotted as a function of the hinge rotation ψ in Fig. 6b for the $L = 100$ mm beam. We note from Fig. 5b that the deformation mode comprises plies shearing past each other as the plies rotate collectively. Thus, the deformation mode is almost incompressible, and is reminiscent of 'kink band folds' in geological formations, see for example Faill (1973) and Price and

Cosgrove (1990). Note too that the microbuckling is at the ply level rather than on the scale of individual fibres. An analytical model to describe the kinematics of the wedge-shaped kink is presented in Appendix A.

This description of a plastic hinge suggests the following strength-of-materials approach. Assume that the composite behaves in a linear elastic manner in tension, and 'yields' in compression in an elastic, ideally plastic manner with a compressive strength of σ_b. Then, deep in the plastic range, the neutral section of the beam is close to the top fibre, and the collapse moment per unit thickness of beam is $M_b = (\sigma_b h) h/2 = \sigma_b h^2/2$. Upon substituting $M_b = 200$N from Fig. 4, and h = 6mm, we obtain an average microbuckling strength of σ_b = 11 MPa.

3. Finite element analysis of the HB26 composite cantilever beam

The above experiments motivate a numerical challenge: what level of fidelity is required in a finite element simulation in order to reproduce the dependence of cantilever beam strength and collapse mode upon beam length? Both of the observed collapse modes involve inter-ply plastic shear and elastic deformation of the plies. We shall simulate these aspects within a finite element (FE) model by making use of cohesive zones between elastic plies. The details are as follows.

3.1 Description of the finite element model

A two dimensional finite element analysis was performed out using the explicit version of the commercial finite element software ABAQUS (version 6.8). The HB26 composite beam consists of 98 unidirectional plies with alternating 0^o and 90^o fibre orientations, see Fig. 7. Our focus is on the prediction of the shear mode of collapse at short beam lengths and plastic hinge formation at long beam lengths. Detailed calculations were performed on beams of length L=10mm in order to simulate the shear mode, and on beams of length L=100mm in order to simulate the bending mode.

Preliminary calculations revealed that the microbuckling mode for the plastic hinge observed in the long beam (L=100mm) requires the presence of an initial geometric imperfection in the form of waviness of the plies. To achieve this, the end portion of the beam (adjacent to the

built-in end) was rotated through an imperfection angle $\left(0 \le \bar{\phi} \le 10^{o}\right)$. This rotated portion extended over a length of $\lambda = 80t$ where t=60μm is the ply thickness. A parametric study is given below in order to determine the sensitivity of the deformation and collapse mode upon $\left(\bar{\phi}, \lambda\right)$.

Each ply was modelled by four-noded plane strain elements with reduced integration (CPE4R in ABAQUS notation). A mesh sensitivity analysis revealed that two elements per ply sufficed for the depth direction of the beam, with suitable grading of the mesh along the length of the beam to make it finest near the built-in end. Orthotropic properties were assigned to the elements, as detailed below. Four-noded cohesive elements (COH2D4 in ABAQUS notation) were placed between adjacent plies to allow for delamination; consequently, the mesh was comprised of 97 layers of cohesive elements connecting 98 plies. In the simulations, the beam was subjected to an increasing transverse displacement near its free end via a rigid, frictionless circular roller of diameter d=6.4mm, see Fig. 7. Contact between the roller and the beam was modelled by the hard, frictionless contact option in ABAQUS. The displacement rate of the roller was chosen to be sufficiently small for inertial effects to be negligible.

3.2 Material properties of the solid and cohesive elements

Take the 1, 2 and 3 directions to lie along the longitudinal axis of the beam, depth direction and width direction, respectively. The plane strain elements are endowed with orthotropic elastic properties as listed in Table 1; the moduli of the elements and the stiffnesses of the interface elements (that is, the cohesive zones) are chosen in order to give the measured effective moduli of the cross-ply composite. For the 0^{o} plies, E_1 equals twice the measured flexural modulus of the beam; E_2 equals three times the shear modulus; and G_{12} equals twice the shear modulus of the laminate.

An elastic-plastic traction-separation law was used for the cohesive elements, such that the elastic separation U_n^{el} in the normal direction and U_s^{el} in the shear direction are linear in the normal traction T_n and shear traction T_s, respectively, according to

$$U_n^{el} = T_n / k_n \qquad \text{and} \qquad U_s^{el} = T_s / k_n \qquad (3)$$

where k_n is the prescribed stiffness of each cohesive layer. The value of k_n is adjusted to ensure that the effective elastic shear modulus of the cross-ply composite equals 50MPa: the choice was made that the solid and cohesive elements contribute equally to both the elastic shear compliance and the normal compliance. (Preliminary simulations show that the response is insensitive to the shear modulus, over the range of 50 MPa to 70 MPa.)

The total separation rates for the elastic-plastic traction-separation law is written as the sum of an elastic part and a plastic part,

$$\begin{cases} \dot{U}_n = \dot{U}_n^{el} + \dot{U}_n^{pl} \\ \dot{U}_s = \dot{U}_s^{el} + \dot{U}_s^{pl} \end{cases} \tag{4}$$

A visco-plastic power law relation is used to describe the plastic separation rates:

$$\begin{cases} \dot{U}_n^{pl} = \dot{U}_0 \left(\frac{T_e}{T_0}\right)^{n-1} \frac{\langle T_n \rangle}{T_0} \\ \dot{U}_s^{pl} = \dot{U}_0 \left(\frac{T_e}{T_0}\right)^{n-1} \frac{T_s}{T_0} \end{cases} \tag{5}$$

where $\dot{U}_0$ and n are a reference separation rate and exponent, respectively, and the effective traction is defined as $T_e = \sqrt{\langle T_n \rangle^2 + {T_s}^2}$. The use of the Macaulay bracket $\langle\rangle$ implies that compressive separation rates vanish. $T_0(U_e^{pl})$ is the cohesive zone law in terms of the flow traction at an equivalent plastic separation U_e^{pl}. Note that the plastic separation is specified in rate form by $\dot{U}_e^{pl} = \sqrt{\left(\dot{U}_n^{pl}\right)^2 + \left(\dot{U}_s^{pl}\right)^2}$. In order to simulate a rate-insensitive quasi-static response, a small value of reference separation rate ($\dot{U}_0$=0.001m/s) and a large value of exponent (n =10) were used in the FE analyses. The assumed softening cohesive law $T_0(U_e^{pl})$ is shown in Fig. 8 and this was implemented for the cohesive elements. This choice of traction-separation curve was determined via an independent set of shear tests on Dyneema specimens, see Appendix B.

3.3 The predicted response for the short beam

The predicted collapse response of a short beam (L =10 mm) is given in Fig. 9a for an imperfection length of λ=40t and selected values of imperfection angle $\bar{\phi}$. Similarly, the response is given in Fig. 9b for $\bar{\phi}$ = 5^o and for selected values of λ. For comparison purposes, the measured collapse response is included in both figures. It is clear that the predicted response is only mildly sensitive to the presence of an imperfection, and the observed strength is adequately modelled by the perfect geometry, $\bar{\phi}$ =0^o. In all cases the predicted response is almost linear elastic followed by a peak load and then a mild drop in load with ensuing displacement. The deformed shape of the beams at a deflection of 3.4mm is given in Fig. 9c for the values of imperfection reported in Fig. 9a (with λ=40t); likewise, the deformed shapes are shown in Fig. 9d for the imperfections reported in Fig. 9b (with $\bar{\phi} = 5^o$). The predicted deformed shape of the short beam is only mildly sensitive to the magnitude of initial imperfection, and the predictions are in reasonable agreement with the observed shape.

3.3 The predicted response for the long beam

A similar parametric study on imperfection sensitivity has been performed for the bending collapse of a long beam (L=100mm), see Fig. 10. Again, the measured response is included in the plots. In contrast to the shear response of the short beam, the bending response of the long beam is sensitive to the misalignment angle $\bar{\phi}$, as shown in Fig. 10a. The peak load is significantly over-estimated for the ideal geometry, $\bar{\phi} = 0^o$, whereas an imperfection on the order of $\bar{\phi} = 5^o$ brings the prediction into approximate alignment with the measured collapse response. For this value of misalignment angle, the peak load is almost insensitive to the imperfection wavelength, see Fig. 10b. However, the precise location of the plastic hinge shifts as λ is increased from 40t to 80t: the longer wavelength causes the hinge to move along the beam and away from the root, see Fig. 10d. The experiments revealed that the precise location of the hinge varied randomly in support of the notion of random imperfections. The rotational nature of the hinge, along with the local bulge formed on the compressive face of the beam due to the wedge-shaped microbuckles are evident in Fig. 10c, regardless of the choice of initial imperfection.

The sensitivity of peak load to the imperfection angle $\bar{\phi}$ is compared for the short and long beams in Fig. 11, for λ=40t. As already remarked, the collapse mode of kinking of the long beam is much more imperfection sensitive than the mode of longitudinal shear in the short beam. In order to bring the predicted failure loads into alignment with the measured loads for both short and long beams, an imperfection angle of 2^o-5^o is appropriate. In subsequent calculations, we shall assume $\bar{\phi}$ =5^o and λ =40t unless otherwise stated.

4. Sensitivity of predicted kinking pattern in long beams to constitutive assumptions

In the above finite element study, the composite beam is discretised into its constituent 0^o and 90^o plies and interfaces, and the appropriate orthotropic elastic constants are ascribed to each of the plies. It is instructive to determine the sensitivity of the collapse load and collapse mode to the interlaminar shear strength. Recall that the overall effective shear compliance of the laminate is the sum of the compliances of the plies and interfaces. We shall also show below that the microbuckling response of the long beam is sensitive to the *partitioning* of the shear compliance between plies and interfaces, at fixed overall, effective value.

For present purposes, it suffices to replace the end-loaded long beam by a short beam subjected to pure bending. In this manner, the size of the finite element mesh is significantly decreased. An increasing end rotation ψ is applied to the free end of an encastre beam of length 20mm, and the work-conjugate moment M is determined. In order to trigger the observed microbuckling mode an initial ply misalignment was introduced near the fixed end with an imperfection angle of $\bar{\phi}$ =5^o and imperfection length λ =40t.

A sensitivity analysis has been performed in order to determine the sensitivity of the bending-collapse response of the beam to the longitudinal shear modulus G_{12} of the plies and to the peak interlaminar strength τ_0. As mentioned above, the idea is to hold the overall, effective shear modulus of the combined plies and interfaces fixed at 50 MPa, and to vary the shear stiffness of the interfaces to compensate for any change in shear modulus of the plies. The shear modulus of the plies was perturbed to the values of 50 MPa and 1000 MPa, in addition to the reference value of 100 MPa. Likewise, the shear strength of the interfaces was perturbed from the reference value of τ_0=2 MPa, such that τ_0=0.2 MPa and 20 MPa.

4.1 Predictions

The moment versus rotation collapse responses and the deformed mesh at a rotation of ψ=10^o are given in Fig. 12 for selected values of interlaminar shear strength τ_0, and in Fig. 13 for selected values of shear modulus of the plies. We conclude that the peak collapse moment, and the collapse mode are sensitive to both the interlaminar shear strength (Fig. 12) and ply shear modulus (Fig. 13), as follows.

(i) A drop in the shear strength leads to a drop in the collapse moment and to an increase in wavelength of the hinge. An increase in the shear strength results in an increase in the collapse moment and to a change in the deformation mode: the wedge-shape kink band is now replaced by a kink at root of the beam on the compressive side more reminiscent of the usual parallel-side microbuckle. On the other hand, a drop in shear modulus of the plies (at fixed effective shear modulus of the composite comprising plies and interfaces) also leads to a drop in the collapse moment and the bulge on the compressive side of the beam is no longer sinusoidal.

(ii) An increase in shear modulus of the plies increases the collapse moment, and switches the collapse mechanism to a diffuse, sinusoidal buckling pattern rather than the wedge-shaped kinks. We conclude that continuum elements of appropriate shear modulus (or, equivalently, a Timoshenko beam or Mindlin plate description with the correct shear modulus) is needed in order to capture the observed kinking mode.

The wedge-shaped kink bands of the present study is in sharp contrast to the more usual parallel-side microbuckle bands that form in composite laminates under uniform compression. The parallel-sided microbuckle bands have been exhaustively studied in the literature, see for example the reviews of Fleck (1997), Kyriakides and Ruff (1995), Kyriakides et al (1997), and Schultheisz and Waas (1996). In conventional plastic microbuckling, the fibres bend elastically in a co-operative manner and the intervening matrix shears plastically. The resulting microbuckle band typically has a width on the order of 20 fibre diameters, see for example Fleck (1997) and Fleck et al (1995). In contrast, the wedge-shaped kink bands of the present study involve both bending and longitudinal shear of the elastic plies, and plastic shear of the intervening inter-ply interfaces.

5. Concluding remarks

The present study highlights the collapse mechanisms for a Dyneema® laminated plate in bending. It is observed that short beams collapse by interlaminar shear, whereas a long beam collapses by a wedge-shaped kinking mechanism. The double-wedge mechanism is kinematically admissible as it gives rise to a rotational hinge, and is strikingly different from the more common case of a parallel-sided kink band, for a long fibre composite under remote compression. We have demonstrated that the wedge-shaped kinking mechanism requires both a low shear strength and a low shear modulus, in order to promote a narrow hinge at the apex of the wedge. Further studies are required in order to map out the competing kinking mechanisms as a function of material and geometric properties as well as the loading conditions.

The finite element analysis of the present study has demonstrated that the wedge-shaped double kink mechanism involves interlaminar shear, along with elastic shear and elastic bending of the intervening plies. Independent measurements of the interlaminar shear response are used in order to make the finite element predictions, by making use of a new form of shear test.

Acknowledgments

This research was supported by the Office of Naval Research (ONR NICOP grant number N00014-09-1-0573). The program manager was Dr David Shifler. MDT was partially supported by ONR grant number N00014-10-1-0415. The authors wish to thank DSM Dyneema for supplying the HB26 laminate plates, and technical discussion facilitating the experimental programme. Dyneema® is a trademark of DSM. Finally, the authors wish to thank Mr. Alan Heaver for his help with the experimental studies.

References

ASTM Test Method D 2344/D 2344M-00. Standard Test Method for Short-Beam Strength of Polymer Matrix Composite Materials and Their Laminates.

ASTM D7264 / D7264M - 07. Standard Test Method for Flexural Properties of Polymer Matrix Composite Materials

Faill, R.T. (1973). Kink-Band Folding, Valley and Ridge Province, Pennsylvania, Geological Society of America Bulletin, **84**(4), 1289-1314.

Fleck, N A. Compressive failure of fibre composites. *Advances in Applied Mechanics*, **33**, 43-119, Academic Press, 1997.

Fleck NA, Deng L and Budiansky B (1995). Prediction of kink width in compressed fibre composites.J. Applied Mechanics,62(2), pp 329-337.

Greenhalgh, E.S., Bloodworth, V.M. Iannucci, L. and Pope, D. (2012). Fractographic Observations on Dyneema® Composites under Ballistic Impact. *Composites Part A*: *: Applied Science and Manufacturing.*

Grujicic, M., Glomski, P. S. , He, T., Arakere, G., Bell, W. C. and Cheeseman, B.A. (2009). Material Modeling and Ballistic-Resistance Analysis of Armor-Grade Composites Reinforced with High-Performance Fibers, *J. Materials Engineering and Performance*, **18**(9), 1169-1182.

Hull, D., and Bacon, D.J. (2011). *Introduction to Dislocations*, Butterworth-Heinemann, 5th Edition. ISBN-9780080966724.

Iannucci, L. and Pope, D. (2011). High velocity impact and armour design, *eXPRESS Polymer Letters* 2011, 5(3)*,* 262–272.

Iannucci L. and Willows M. (2006). An energy based damage mechanics approach to modelling impact onto woven composite materials – Part I: Numerical models. *Composites Part A: Applied Science and Manufacturing*, **37**, 2041–2056.

Kyriakides, S., and Ruff, A.E., (1997). Aspects of the failure and postfailure of fiber composites in compression. *J. of Composite Materials*, **31**, 2000-2037.

Kyriakides, S., Arseculeratne, R., Perry, E.J. and Liechti, K.M. (1995). On the compressive failure of fiber reinforced composites. *Int. J. Solids Structures*, **32**, 689-738.

Price, N.P. and Cosgrove, J. W. (1990). Analysis of Geological Structures, Cambridge University Press.

Russell, B.P., Kandan, K., Deshpande, V.S. and Fleck, N.A. (2013). The high strain rate response of UHMWPE: from fibre to laminate, *Int. J. Impact Engng.*, **60**, 1-9.

Schultheisz, C.R. and Waas, A.M. (1996). Compressive failure of composites, Part I: testing and micromechanical theories. *Progress in Aerospace Sciences*, **32**, 1-42.

Utomo, B.D.H. and Ernst, L.J. (2008). Detailed modelling of projectile impact on dyneema composite using dynamic properties, *J. Solid Mechanics and Materials Engineering*, **2**(6), 707-717.

Tables

Table1. Elastic properties of the solid elements

	E_1 (GPa)	E_2 (GPa)	v_{12}	G_{12} (GPa)
0^o ply	68	0.15	0.3	0.1
90^o ply	0.15	0.15	0.3	0.1

Appendix A. Analytical model for hinge formation by plastic kinking

An analytical model is now detailed for the plastic hinge in a laminated or unidirectional fibre composite: the hinge comprises two wedge-shaped kink bands, see Fig. A1. Consider a beam, with each arm bent through an angle ψ about a central hinge. The beam is idealised as a smeared-out stack of inextensional rigid layers, and intervening rigid, ideally plastic matrix of shear yield strength *k*. We shall assume that kinking is by plastic shear of the layers in a volume-conserving manner.

At any instant, the beam comprises the following zones of uniform deformation:

(i) Each end of the beam undergoes rigid-body rotation by $\pm\psi$

(ii) In two wedge-shaped zone of the active hinge, the layers rotate though an angle of $\pm\phi$.

In order for hinge rotation to conserve volume, the boundaries OB, OC and OD behave like twin-boundaries in a crystalline solid (Hull and Bacon, 2011), such that $\phi = 2(\beta + \psi)$, where β is the wedge angle as defined in Fig. A1. Additionally, conservation of volume dictates that the angles β and ψ are related via

$$\cot(\beta+\psi) = \left[\cos(2\beta+\psi)\cot\beta + \sin(2\beta+\psi)\right]\cos(2\beta+\psi) \qquad \text{(A1)}$$

The moment-rotation $M-\psi$ collapse response is determined by the following work argument. Consider the left-hand side of the beam. Then, the external work is $W^P = \int_0^{\psi} M(\psi')d\psi'$ while the internal work done within the wedge OBC of area $A = \frac{1}{2}h^2\tan(\beta+\psi)$ involves the shear stress *k* working through the uniform shear strain of magnitude $2(\beta+\psi)$ within the wedge, to give

$$W^P = 2(\beta+\psi)kA \qquad \text{(A2)}$$

Now equate the external and internal work rates to obtain

$$\dot{W}^P = M\dot{\psi} = 2(\beta+\psi)k\dot{A} + 2(\dot{\beta}+\dot{\psi})kA \qquad \text{(A3)}$$

Since $\dot{A}$ and $\dot{\beta}$ are linear in $\dot{\psi}$, the above relation (A3) gives the bending moment *M* for any assumed value of beam rotation ψ. To see this, first note that (A1) is an implicit function for β in terms of ψ. Time differentiation of (A1) gives

$$f_1(\beta,\psi)\dot{\beta} + f_2(\beta,\psi)\dot{\psi} = 0 \qquad \text{(A4)}$$

where

$$f_1(\beta,\psi) = -2\text{cosec}^2(\beta+\psi) + \text{cosec}^2\beta\left[1+\cos(4\beta+2\psi)\right] + 4\cot\beta\sin(4\beta+2\psi) - 4\cos(4\beta+2\psi) \quad \text{(A5a)}$$

and

$$f_2(\beta,\psi) = -2\text{cosec}^2(\beta+\psi) + 2\cot\beta\sin(4\beta+2\psi) - 2\cos(4\beta+2\psi) \quad \text{(A5b)}$$

Likewise, the rate form of $A = \frac{1}{2}h^2\tan(\beta+\psi)$ reads:

$$\dot{A} = \frac{1}{2}h^2\sec^2(\beta+\psi)\left[\dot{\beta}+\dot{\psi}\right] \quad \text{(A6)}$$

Substitution of (A4) and (A5) into (A3) then gives

$$M = \left[\frac{f_1 - f_2}{f_1}\right]\left[(\beta+\psi)\sec^2(\beta+\psi) + \tan(\beta+\psi)\right]kh^2 \quad \text{(A7)}$$

Comparison with finite element simulations

It is instructive to compare the predictions (A1) and (A7) of the analytical model with those of the full numerical simulations. To make the comparison, an end rotation ψ was applied to the beam in the finite element simulations, and the work-conjugate end moment M was determined. A 'softening law' for the cohesive zones between plies was assumed, with initial peak value 2.0MPa, as shown in Fig. 8. Additionally, a 'perfectly plastic' cohesive zone law was assumed, such that T_0 is held constant at 2.0MPa. The results for these two simulations are compared with the analytical predictions in Fig. A2; to make contact between finite element simulation and analytical model we take the shear strength in the finite element simulations k to equal T_0 (since this is the longitudinal shear strength of the beam).

It is clear that the simple analytical model captures the kinematics of the kink bands (Fig. A2a), except for the early stage of kink band nucleation. Moreover, the comparison between the measured kink kinematics and the predictions of this model are included in Fig. 6b and again show that the model captures the kinematics to a high degree of accuracy except during the early stages. However, the kink band model neglects the elastic bending energy of the layers at the kink boundaries, and thereby underpredicts the moment $M(\psi)$; see Fig. A2b.

Appendix B: The traction-displacement bridging law across an interply delamination under remote shear

B1. Shear tests

Double-notch shear tests were performed on the HB26 laminates, of geometry shown in Fig. B1, in order to measure the interlaminar shear properties. A three hole arrangement was employed in order to generate delamination on two planes as marked by the dotted lines in Fig. B1. The specimen height h was 6mm (see Fig. B1) and the width w (into the page of Fig. B1) was set at 20 mm. The length s of the delamination plane was set at 30 mm. (Preliminary tests confirmed that the shear strength was independent of w and s provided they each exceeded about 10 mm.)

Tests were conducted in a screw-driven test machine by gripping the ends of the specimen in wedge grips. The relative shear displacement across each delamination is measured using a clip gauge; the clip gauge, of span (s=10mm), is mounted on the *side face* of the specimen and spans the holes, see Fig. B1. As such, it is a *remote measure* of the interlaminar displacement jump. The *average shear traction*, acting on the shear planes between the inner large hole and the outer small holes, is determined from the applied load per unit width F and length of ligament s according to

$$\tau = F/2s \qquad \text{(B.1)}$$

We emphasise that the shear tests do not give directly the traction versus displacement characteristic across the delamination, as the displacement measurement is remote from the delamination plane, and only the average traction is measured. To aid interpretation, a finite element analysis is performed with an assumed interface law (local shear traction versus shear displacement jump) for the delamination plane, and the predictions are matched against the measured average traction versus displacement from the measured clip gauge response.

B2. Measured response

The average shear traction versus displacement jump across one of the delamination planes is plotted in Fig. B2a for a cross-head displacement rate of 1 mm/min. Additional insight into the collapse mode was obtained by post-test observation in a 3D X-ray CAT scanning machine, see Fig. B3. Delamination occurs on two distinct shear planes. The magnitude of displacement jump across these shear planes was measured during the tests using Digital Image Correlation (DIC) in addition to use of the clip gauge. To achieve this, a speckle pattern was painted onto the front face of the specimen and the face of the specimen was videoed during testing. Contour maps of the axial displacement field are shown in Fig. B4 at salient points in the test. The displacement jump between the contact points of the clip gauge is extracted from the DIC measurements and used to construct a plot of shear traction versus displacement jump in Fig. B4. The measured load versus clip gauge response is included in the figure and good agreement is noted for the two methods of displacement measurement. (Note that the measured curve included in Fig. B4 differs slightly from that in Fig. B2 as these are different tests and there is some scatter associated with these shear experiments.) Post peak load, shear localization occurs and two shear bands of intense deformation emerge, as witnessed by the DIC contour plots.

B3. Finite element simulations of the triple notch shear test

A two dimensional, plane strain finite element analysis was conducted to calibrate the shear traction versus displacement response of a delamination between plies. Each ply was modelled by four-noded solid elements and cohesive zones placed between all plies similar to the model described in Section 3 of the main text. The elastic properties of the solid and cohesive elements were the same as those used in Section 3 above: each ply was modelled explicitly by an anisotropic elastic layer.

A parametric study was conducted in order to calibrate the cohesive law: three elastic-softening plastic cohesive laws were used with post-peak slope of -40, -20 and -13.3GPa/m (Fig. B2b). Motivated by the observed response as shown in Fig. B2a, a residual strength (0.2MPa) remains after the softening in each cohesive law. The peak cohesive strength was taken to be 2MPa, as set by the collapse load in the short cantilever beam tests.

The predicted average traction versus clip gauge response is given in Fig. B2a. The finite element simulations give delamination on a plane tangential with the edge of the small holes,

in agreement with the observed collapse mode. It is found that the cohesive law II, with post-peak stiffness of -20GPa/m, gave the best fit to the observed response. Accordingly, we make use of this cohesive law in the body of the paper, recall Fig. 8.

Figure Captions

Fig. 1: Sketch of the clamped HB26 composite beam geometry.

Fig. 2: Plot of the measure compliance C of the HB26 composite beam versus beam length L for 3 loading rates $\dot{\delta}$.

Fig. 3: (a) Load per unit width P versus displacement δ responses of short (L=10mm) and long (L=100mm) HB26 composite beams. (b) X-ray and photographs showing the deformation of the short and long beams at applied displacements $\delta = 8$ mm and 25 mm, respectively.

Fig. 4: Collapse load $P_{\max}$ (per unit width) versus HB26 composite beam length L, showing the transition between shear and bending dominated collapse modes.

Fig. 5: Plastic hinge formation by microbuckling in the long beam (L=100mm): (a) Sketch of the double-wedge kind band. In this illustrative sketch, chain lines denote the 0^o plies, and the dotted lines denote the 90^o plies; (b)-(d) images of the kind bands at different magnifications.

Fig. 6: (a) Definition of the kink wedge angle β and beam rotation ψ. In this illustrative sketch, chain lines denote the 0^o plies, and the dotted lines denote the 90^o plies. (b) Measurements of the wedge angle as a function of the beam rotation for the L=100mm HB26 composite beam. Predictions of the model from Appendix A are also included.

Fig. 7: Sketch illustrating the details of the finite element model of the HB26 composite beams. In this illustrative sketch, chain lines denote the 0^o plies, and the dotted lines denote the 90^o plies.

Fig. 8: The softening cohesive zone law used to model the interlaminar of the HB26 composite beam.

Fig. 9: Sensitivity of the response of the short beam (L=10mm) HB26 composite beam to the choice of initial imperfection. The load P per unit width versus displacement δ response for (a) λ =40t, and (b) $\bar{\phi} = 5^{\circ}$. Top and bottom surface profiles of the beam are shown for an end displacement of $\delta = 3.4$mm and choices λ =40t and $\bar{\phi} = 5^{\circ}$ in (c) and (d), respectively.

Fig. 10: Sensitivity of the response of the long beam (L=100mm) HB26 composite beam to the choice of initial imperfection. The load P per unit width versus displacement δ response for (a) λ =40t, and (b) $\bar{\phi} = 5^{\circ}$. Top and bottom surface profiles of the beam are shown for an end displacement of $\delta = 15$mm and choices λ =40t and $\bar{\phi} = 5^{\circ}$ in (c) and (d), respectively.

Fig. 11: Collapse load $P_{\max}$ (per unit width) versus imperfection angle $\bar{\phi}$, for the choice of imperfection length λ =40t.

Fig. 12: Finite element calculations to illustrate the sensitivity of the response of long beams to the interlaminar strength $T_{\max}$. (a) The applied moment M versus rotation ψ. (b) The predicted deformed configurations for three choices of interlaminar strength: (i) $T_{\max} = 0.2$ MPa; (ii) $T_{\max} = 2$ MPa and (iii) $T_{\max} = 20$ MPa. The overall deformed shapes of the beams and magnified views of the bending hinge are shown for an applied rotation $\psi = 10^{\circ}$.

Fig. 13: Finite element calculations to illustrate the sensitivity of the response of long beams to the shear modulus G of the plies. (a) The applied moment M versus rotation ψ. (b) The predicted deformed configurations for three choices of interlaminar modulus: (i) $G = 50$ MPa; (ii) $G = 100$ MPa and (iii) $G = 1000$ MPa. The overall deformed shapes of the beams and magnified views of the bending hinge are shown for an applied rotation $\psi = 10^{\circ}$.

Fig. A1: The assumed plastic hinge: two wedge-shaped kink zones. In this illustrative sketch, chain lines denote the 0° plies, and the dotted lines denote the 90° plies.

Fig. A2: Comparison of finite element predictions with analytical model for (a) the hinge kinematics and (b) load carrying capacity of the hinge. The FE calculations are show for two choices of the cohesive relation.

Fig. B1: The double-notch geometry for measuring the interlaminar shear response of the HB26 composite.

Fig. B2: (a) Nominal shear traction versus displacement jump across the interply shear band as measured via the clip gauge. Finite element calculations using three choices of cohesive relations are included. (b) Sketch illustrating the 3 cohesive relations used in the FE calculations included in (a).

Fig. B3: X-ray image of the double-notch shear specimen in a plane perpendicular to the shear plane. The image was taken after loading the specimen until the clip gauge measured a displacement of 1mm and then unloading. The bands of intense shear between the plies results in some delamination that is clearly seen in this image.

Fig. B4: Measured traction versus displacement relation from the double notch shear specimen. The displacement is measured via both a clip gauge and using digital image correlation (DIC). (b) Contours of displacement in x-direction on one side of the specimen (perpendicular to the shear planes).

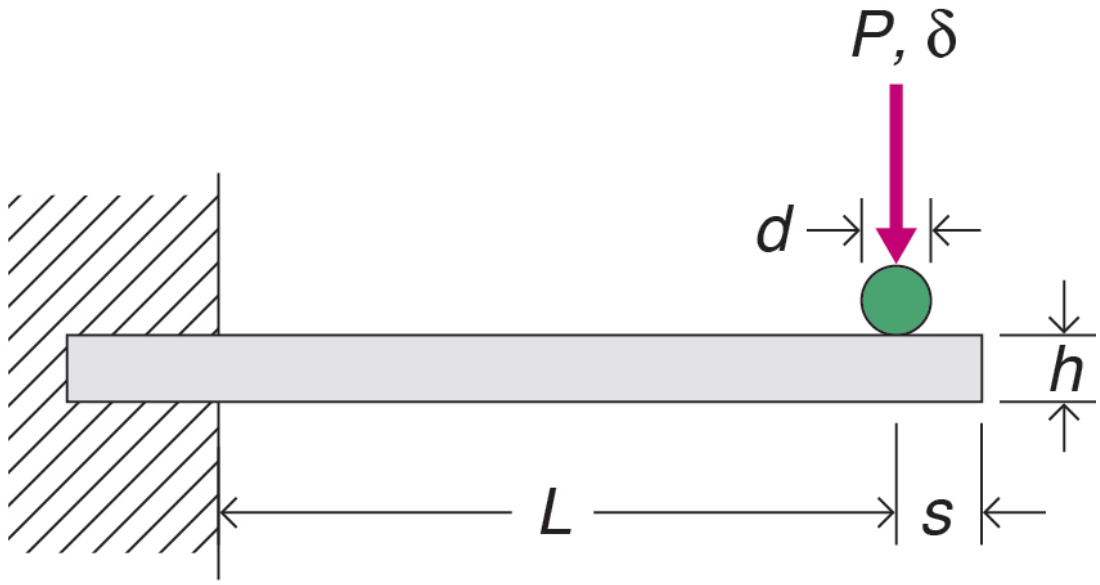

Fig. 1:

Sketch of the clamped HB26 composite beam geometry.

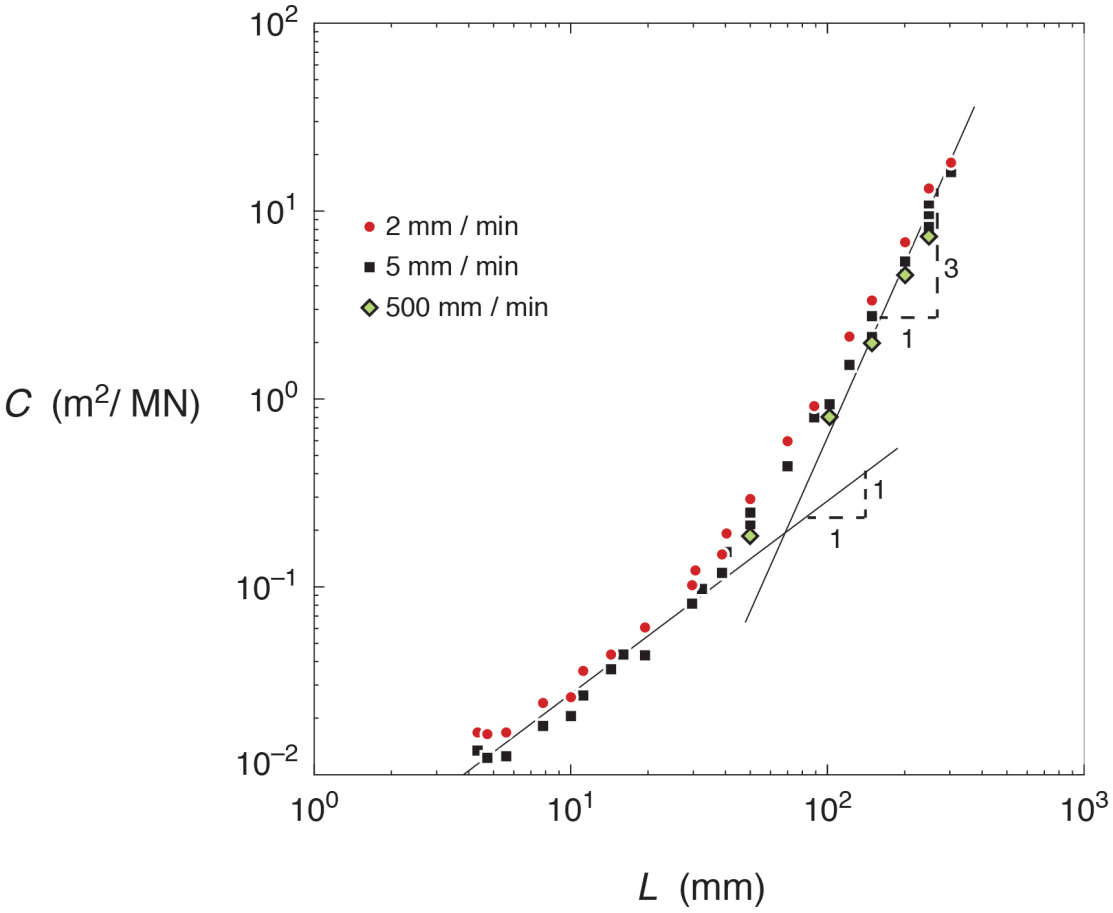

Fig. 2: Plot of the measure compliance C of the HB26 composite beam versus beam length L for 3 loading rates $\dot{\delta}$.

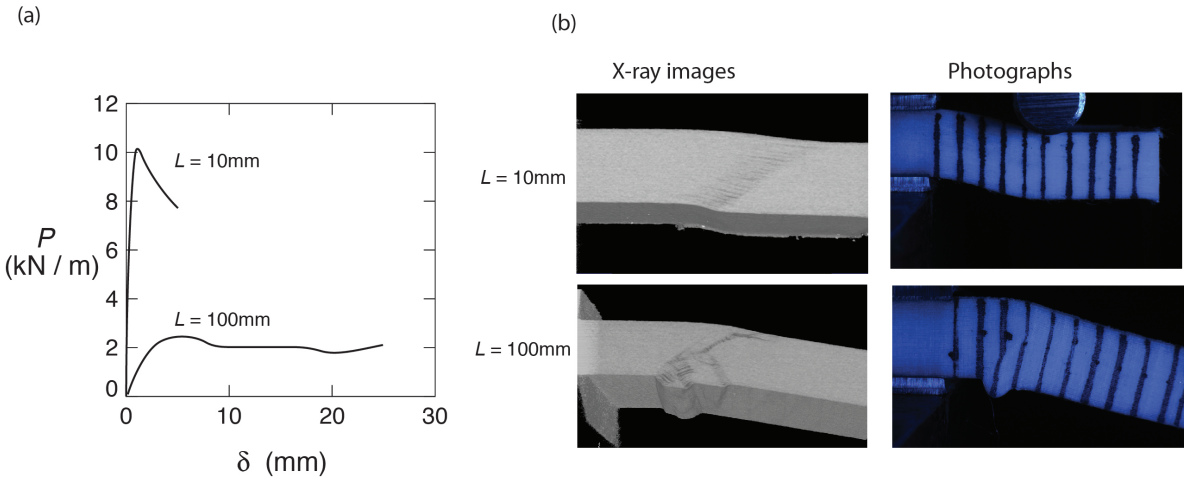

Fig. 3: (a) Load per unit width P versus displacement δ responses of short (L=10mm) and long (L=100mm) HB26 composite beams. (b) X-ray and photographs showing the deformation of the short and long beams at applied displacements $\delta = 8$ mm and 25 mm, respectively.

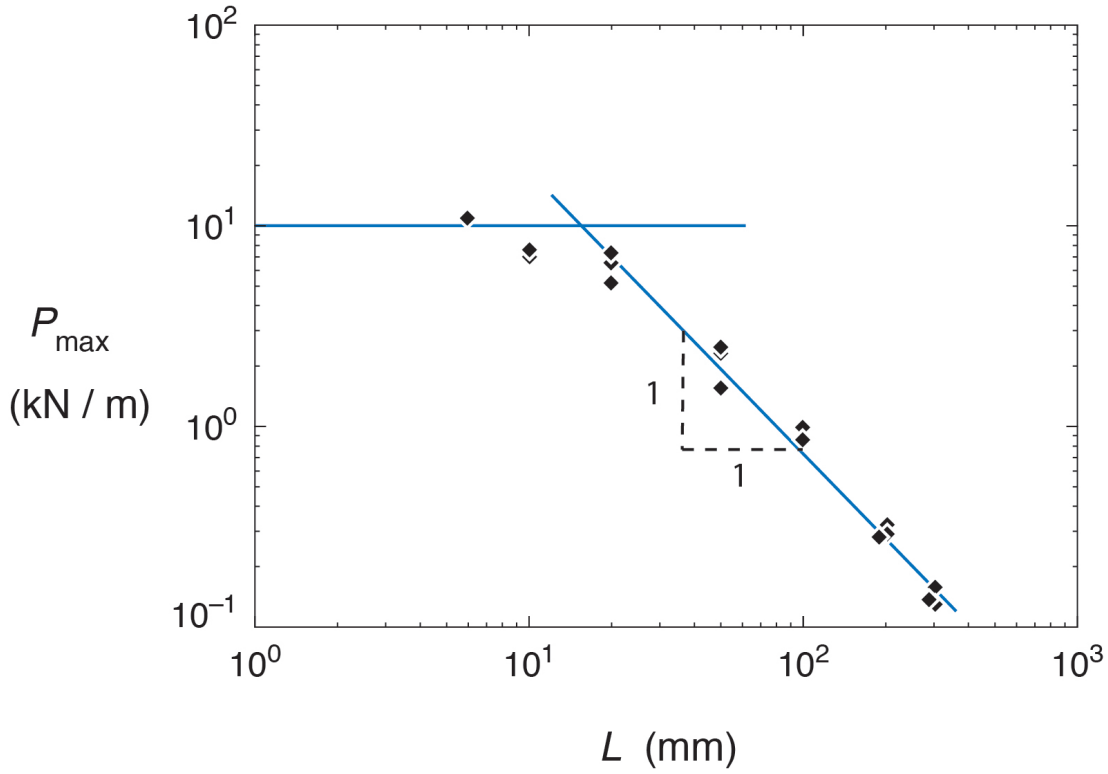

Fig. 4: Collapse load P_{max} (per unit width) versus HB26 composite beam length L, showing the transition between shear and bending dominated collapse modes.

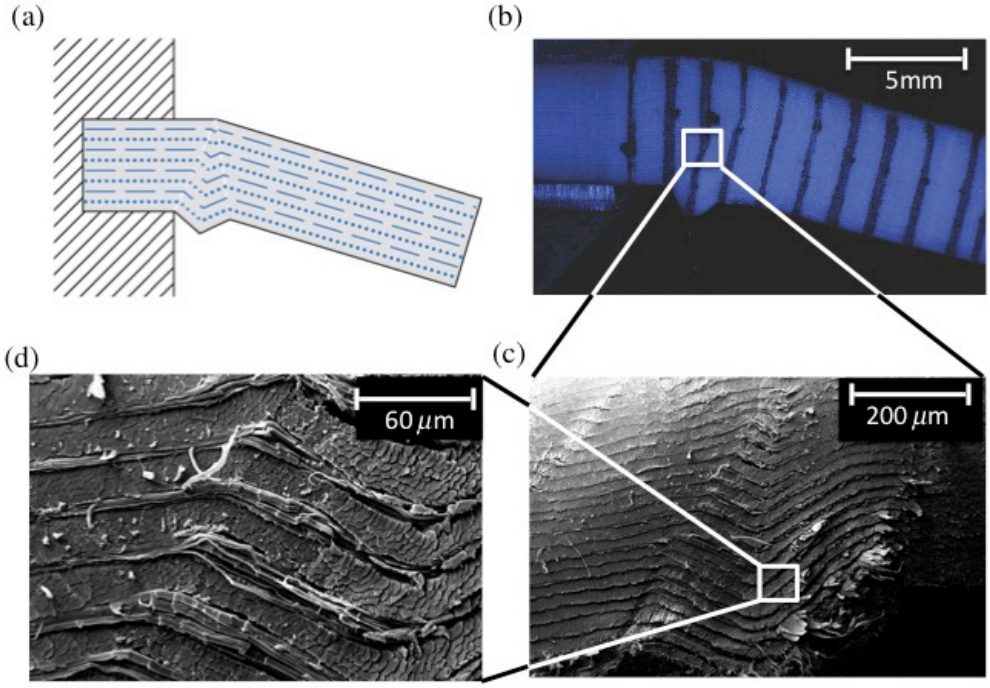

Fig. 5: Plastic hinge formation by microbuckling in the long beam (L=100mm): (a) Sketch of the double-wedge kind band. In this illustrative sketch, chain lines denote the 0^o plies, and the dotted lines denote the 90^o plies; (b)-(d) images of the kind bands at different magnifications.

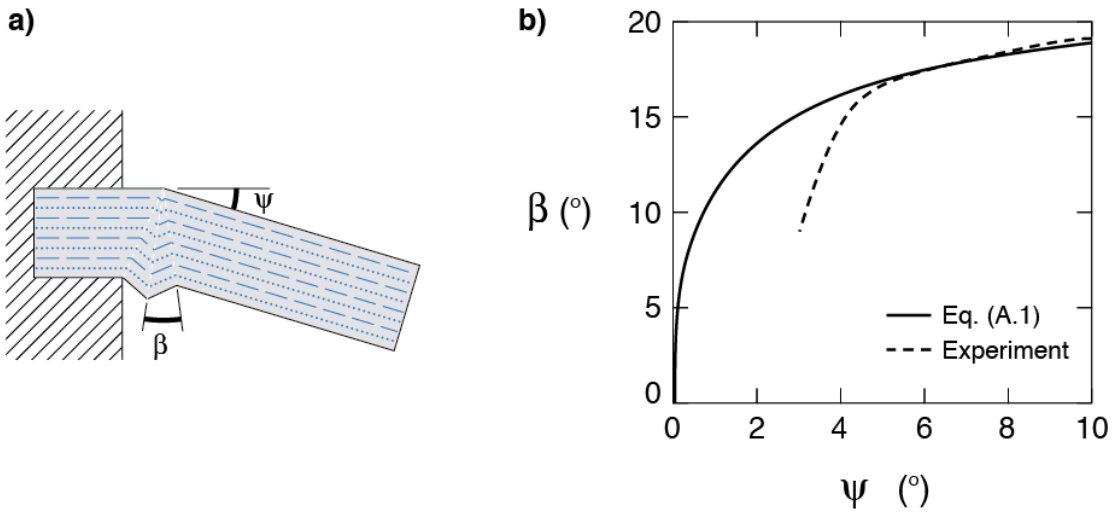

Fig. 6: (a) Definition of the kink wedge angle β and beam rotation ψ. In this illustrative sketch, chain lines denote the 0^o plies, and the dotted lines denote the 90^o plies. (b) Measurements of the wedge angle as a function of the beam rotation for the L=100mm HB26 composite beam. Predictions of the model from Appendix A are also included.

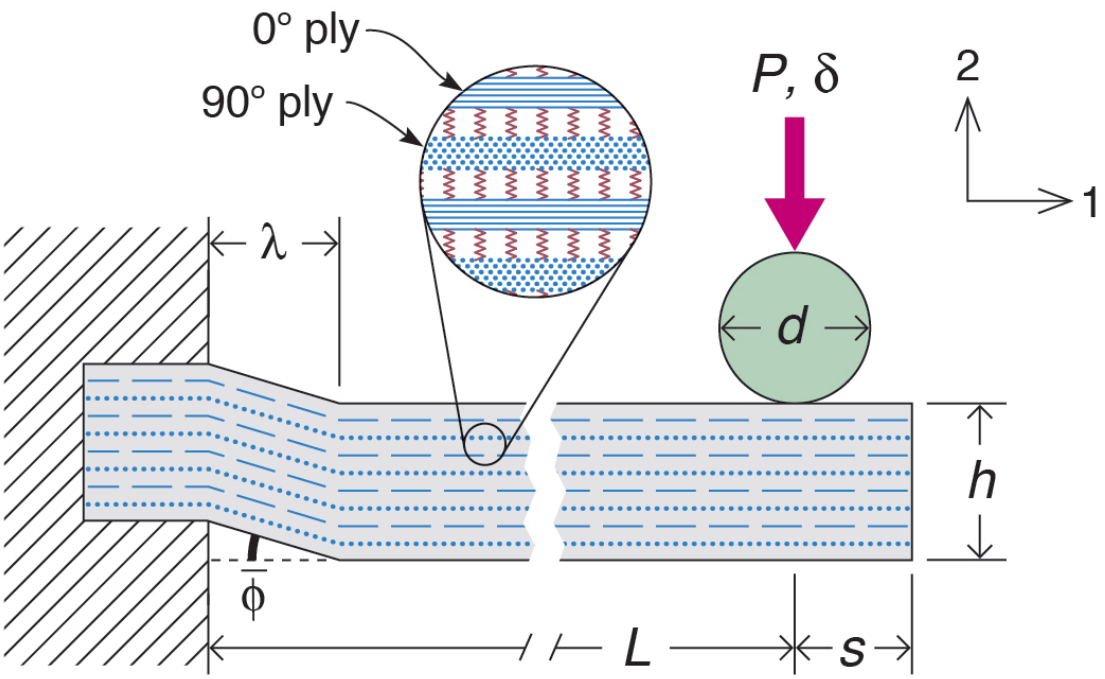

Fig. 7:

Sketch illustrating the details of the finite element model of the HB26 composite beams. In this illustrative sketch, chain lines denote the 0^o plies, and the dotted lines denote the 90^o plies.

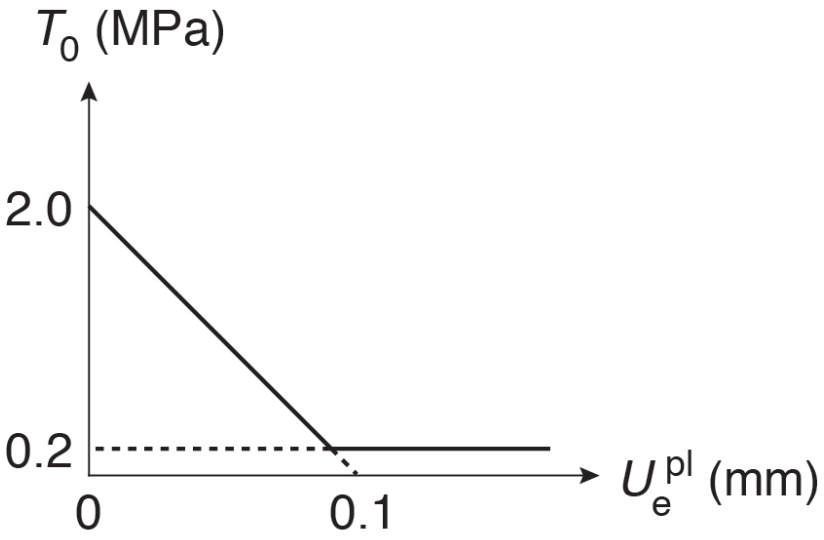

Fig. 8: The softening cohesive zone law used to model the interlaminar of the HB26 composite beam.

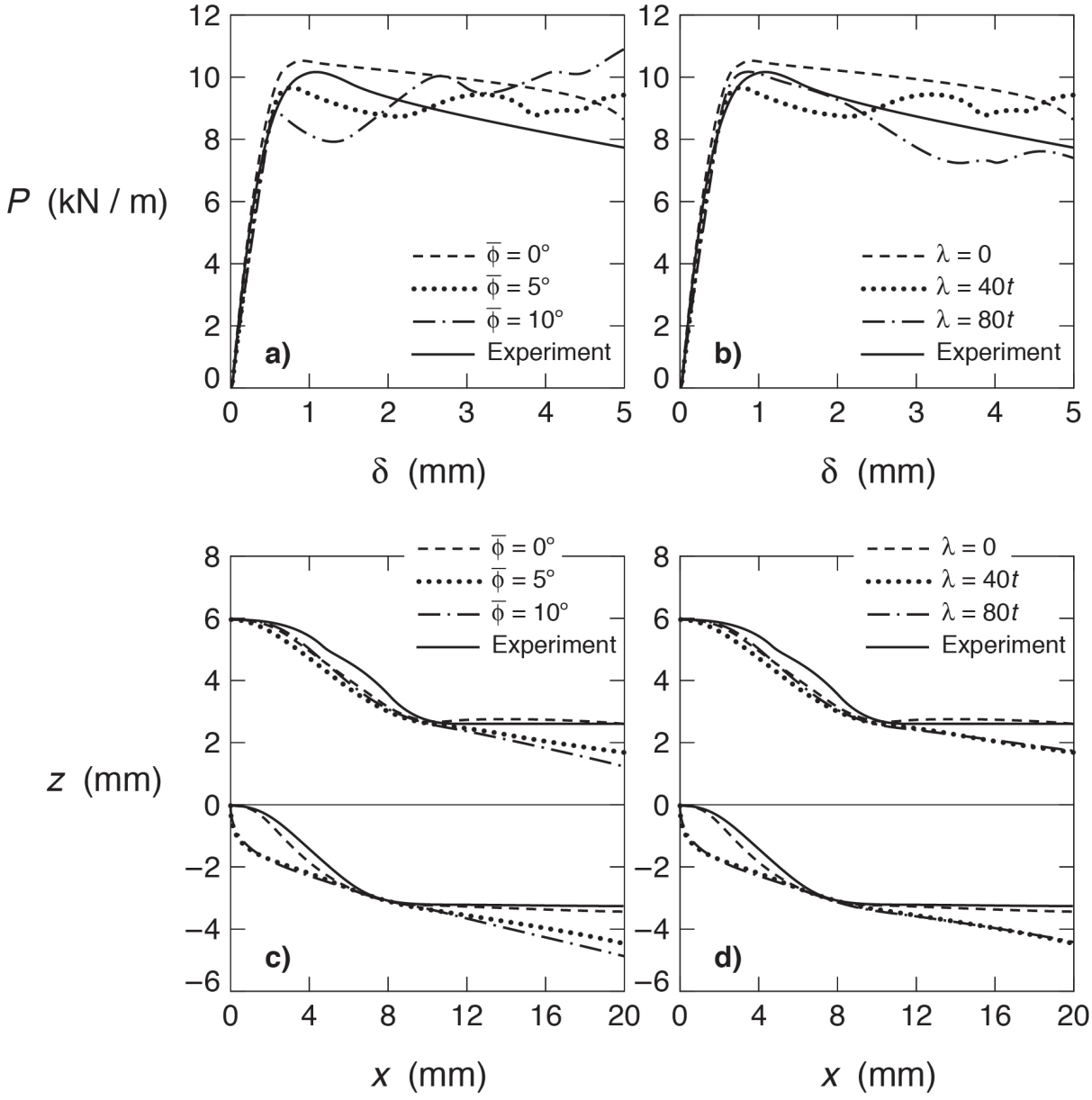

Fig. 9: Sensitivity of the response of the short beam (L=10mm) HB26 composite beam to the choice of initial imperfection. The load P per unit width versus displacement δ response for (a) λ=40t, and (b) $\bar{\phi} = 5^{o}$. Top and bottom surface profiles of the beam are shown for an end displacement of $\delta = 3.4$mm and choices λ=40t and $\bar{\phi} = 5^{o}$ in (c) and (d), respectively.

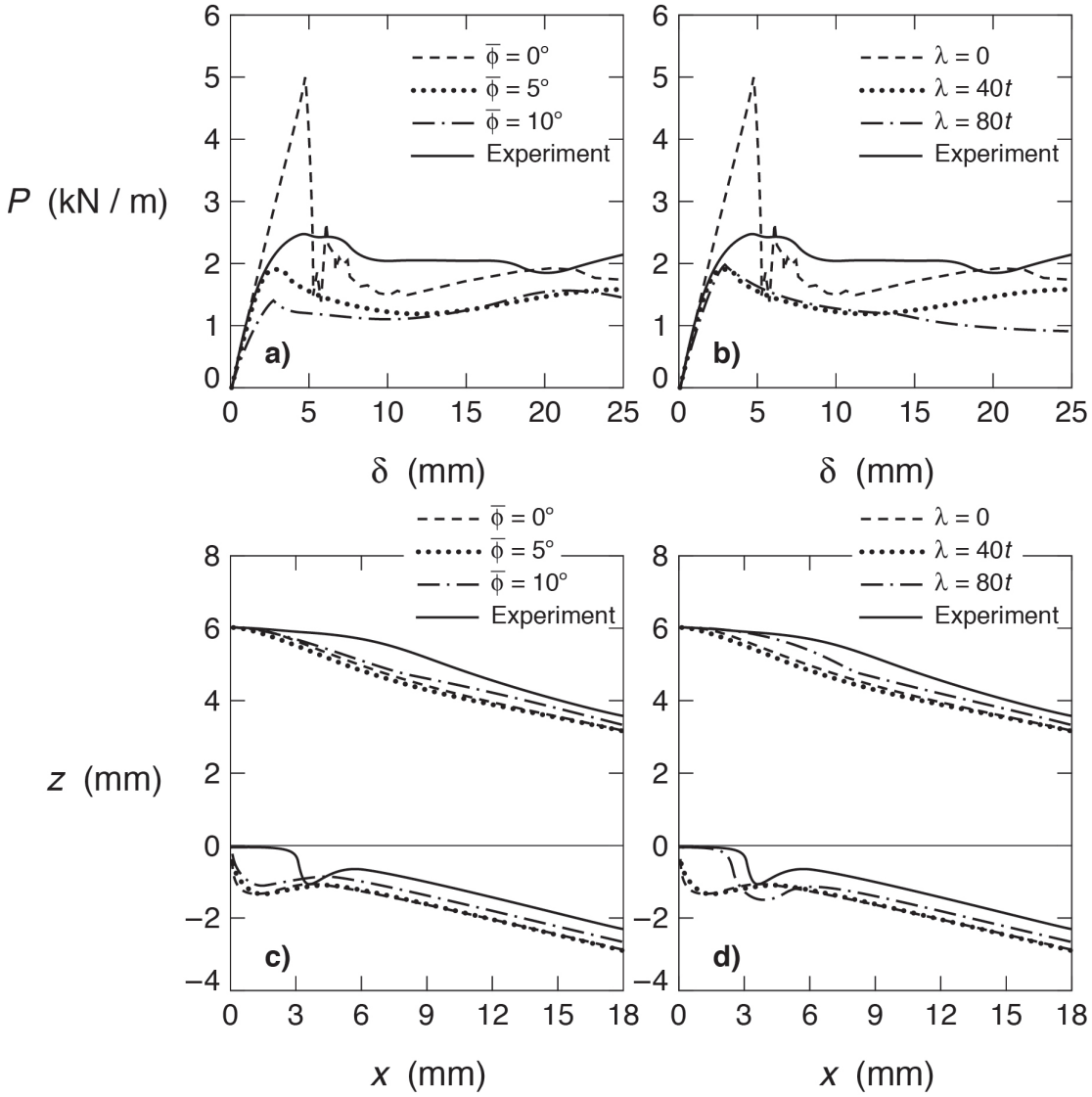

Fig. 10: Sensitivity of the response of the long beam (L=100mm) HB26 composite beam to the choice of initial imperfection. The load P per unit width versus displacement δ response for (a) λ=40t, and (b) $\bar{\phi} = 5^{\circ}$. Top and bottom surface profiles of the beam are shown for an end displacement of $\delta = 15$mm and choices λ=40t and $\bar{\phi} = 5^{\circ}$ in (c) and (d), respectively.

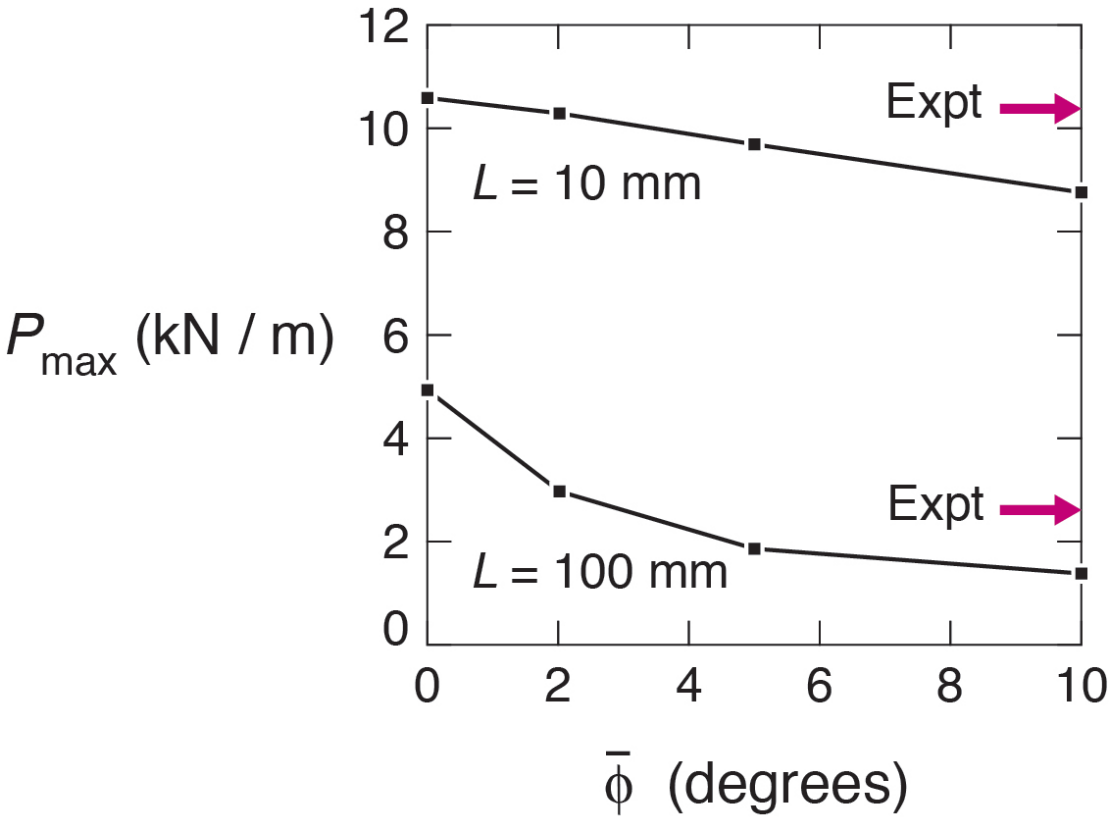

Fig. 11: Collapse load P_{max} (per unit width) versus imperfection angle $\bar{\phi}$, for the choice of imperfection length $\lambda = 40t$.

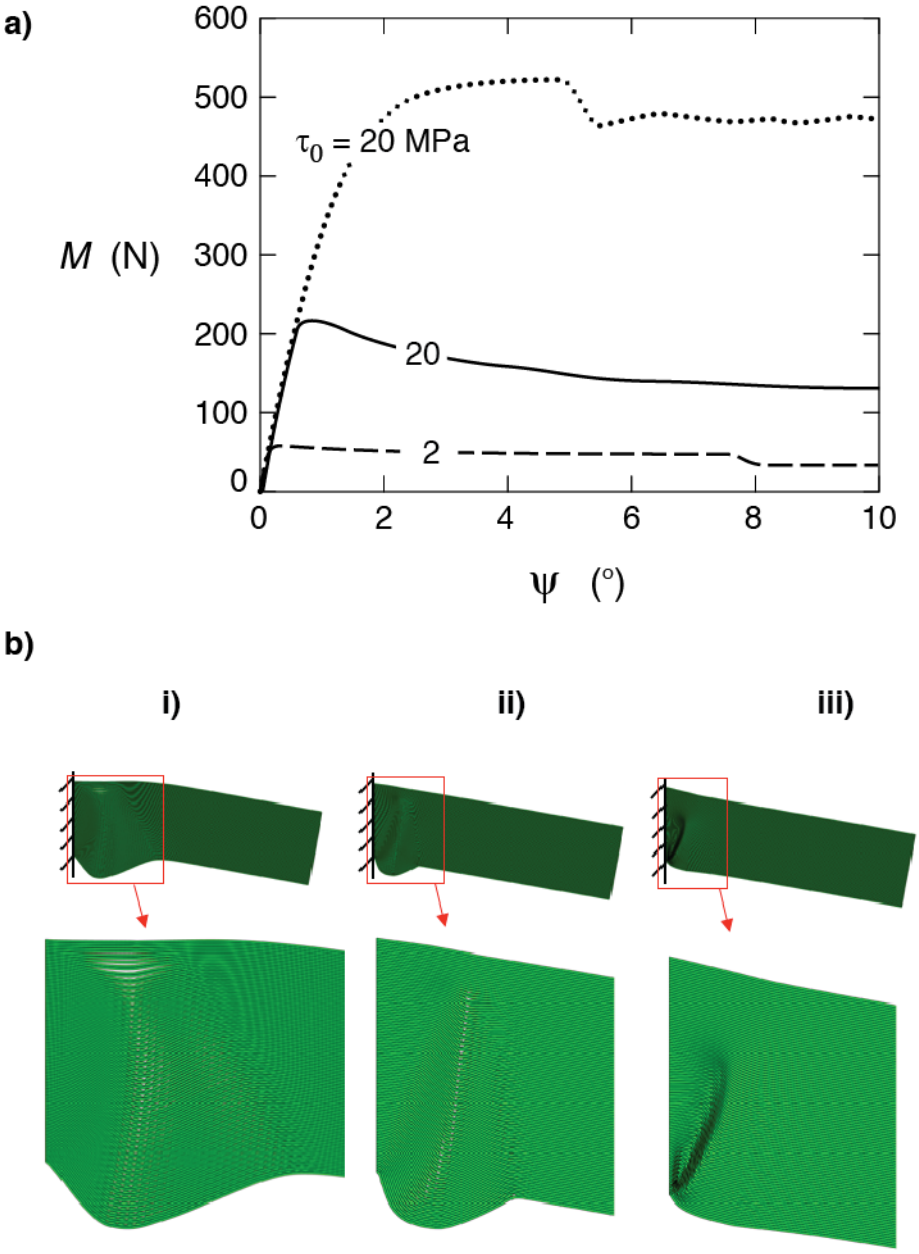

Fig. 12: Finite element calculations to illustrate the sensitivity of the response of long beams to the interlaminar strength $T_{\max}$. (a) The applied moment M versus rotation ψ. (b) The predicted deformed configurations for the three choices of interlaminar strength: (i) $T_{\max} = 0.2$ MPa; (ii) $T_{\max} = 2$ MPa and (iii) $T_{\max} = 20$ MPa. The overall deformed shapes of the beams and magnified views of the bending hinge are shown for an applied rotation $\psi = 10^{o}$.

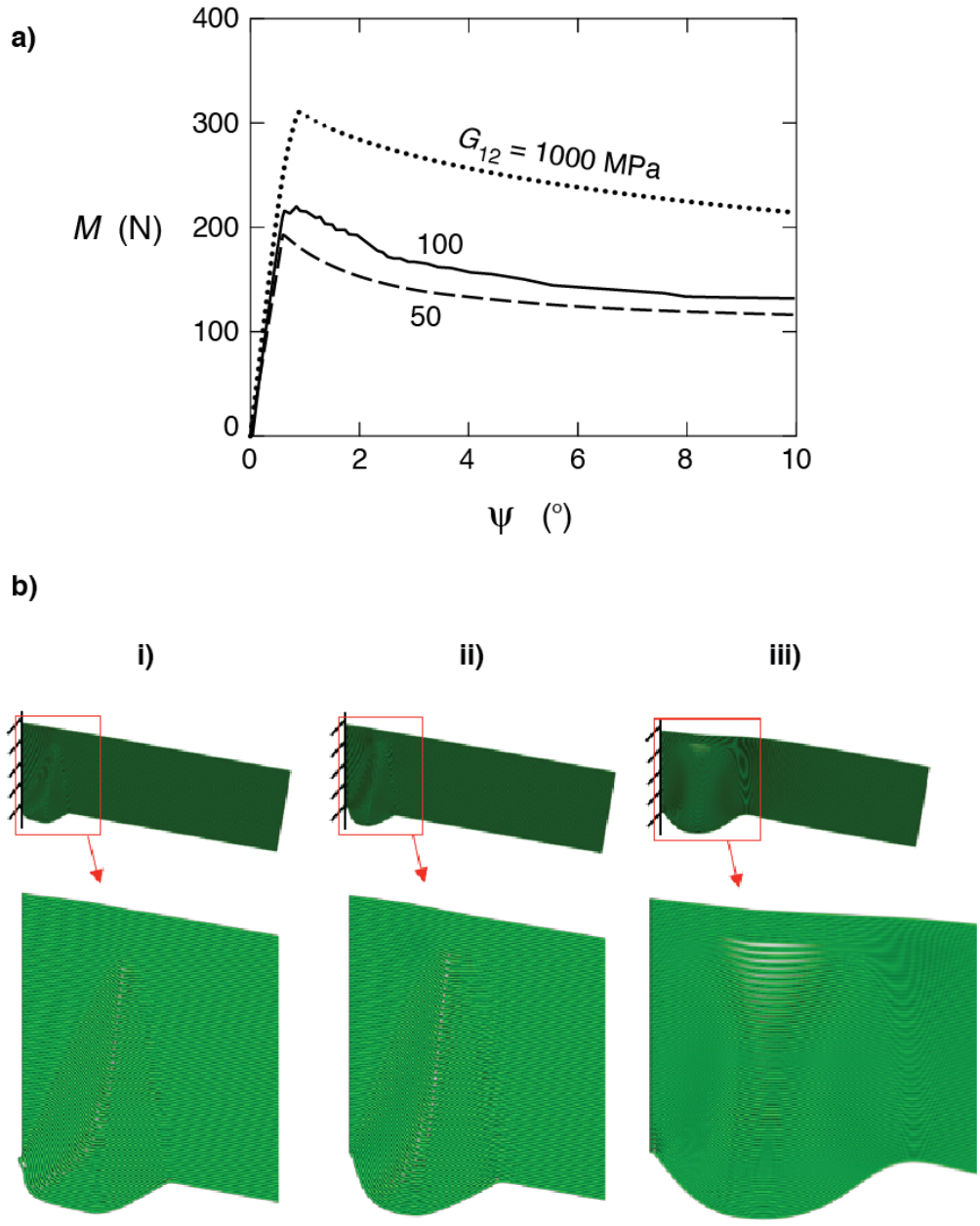

Fig. 13: Finite element calculations to illustrate the sensitivity of the response of long beams to the shear modulus G of the plies. (a) The applied moment M versus rotation ψ. (b) The predicted deformed configurations for three choices of interlaminar modulus: (i) $G = 50$ MPa; (ii) $G = 100$ MPa and (iii) $G = 1000$ MPa. The overall deformed shapes of the beams and magnified views of the bending hinge are shown for an applied rotation $\psi = 10^{o}$.

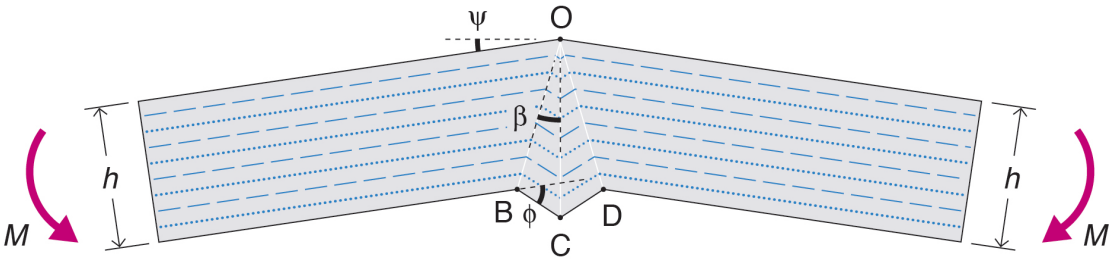

Fig. A1: The assumed plastic hinge: two wedge-shaped kink zones. In this illustrative sketch, chain lines denote the 0^{o} plies, and the dotted lines denote the 90^{o} plies.

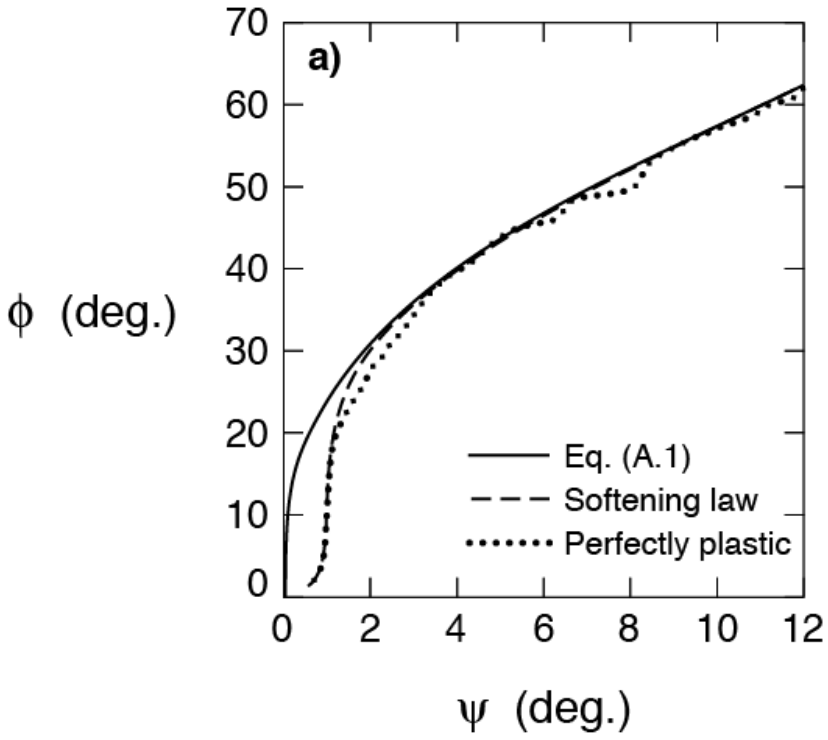

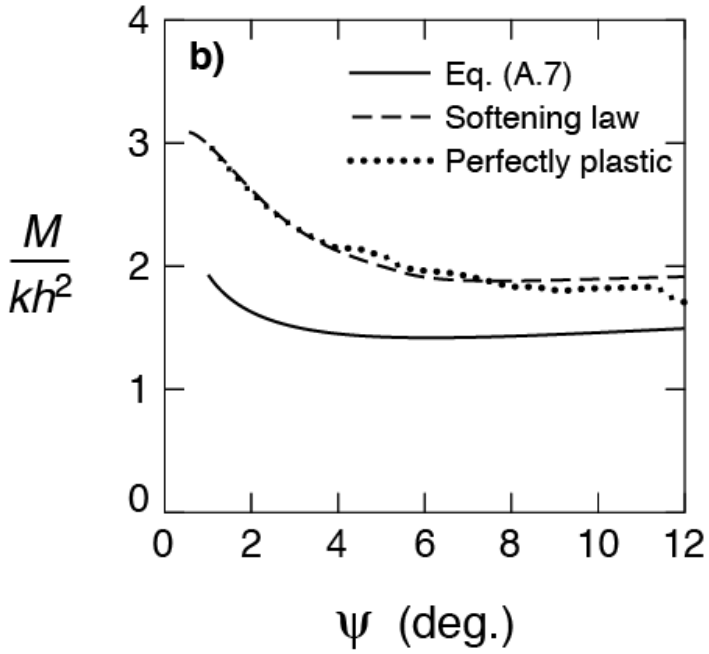

Fig. A2: Comparison of finite element predictions with analytical model for (a) the hinge kinematics and (b) load carrying capacity of the hinge. The FE calculations are show for two choices of the cohesive relation.

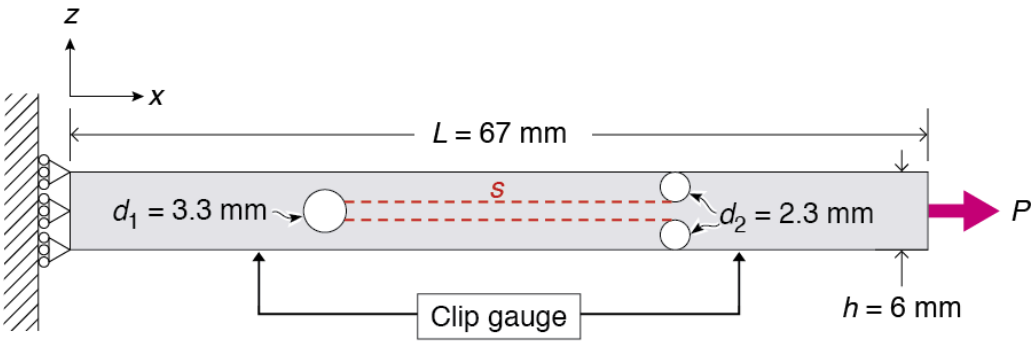

Fig. B1: The double-notch geometry for measuring the interlaminar shear response of the HB26 composite.

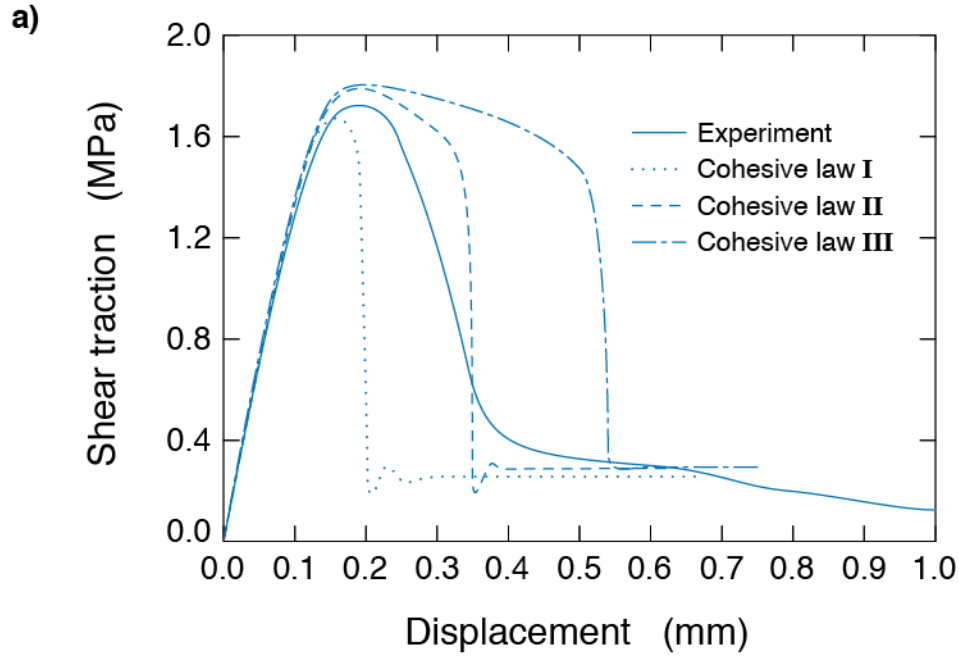

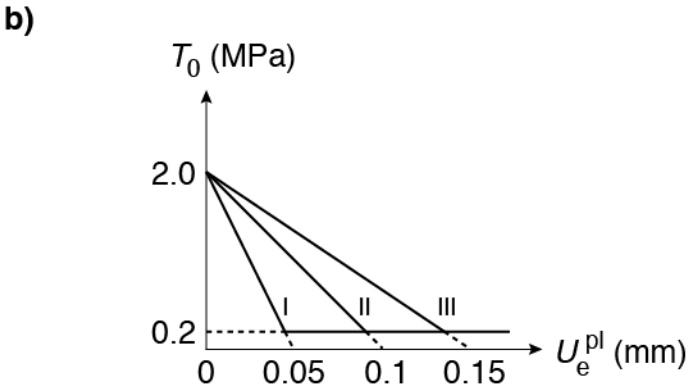

Fig. B2: (a) Nominal shear traction versus displacement jump across the interply shear band as measured via the clip gauge. Finite element calculations using three choices of cohesive relations are included. (b) Sketch illustrating the 3 cohesive relations used in the FE calculations included in (a).

Fig. B3: X-ray image of the double-notch shear specimen in a plane perpendicular to the shear plane. The image was taken after loading the specimen until the clip gauge measured a displacement of 1mm and then unloading. The bands of intense shear between the plies results in some delamination that is clearly seen in this image.

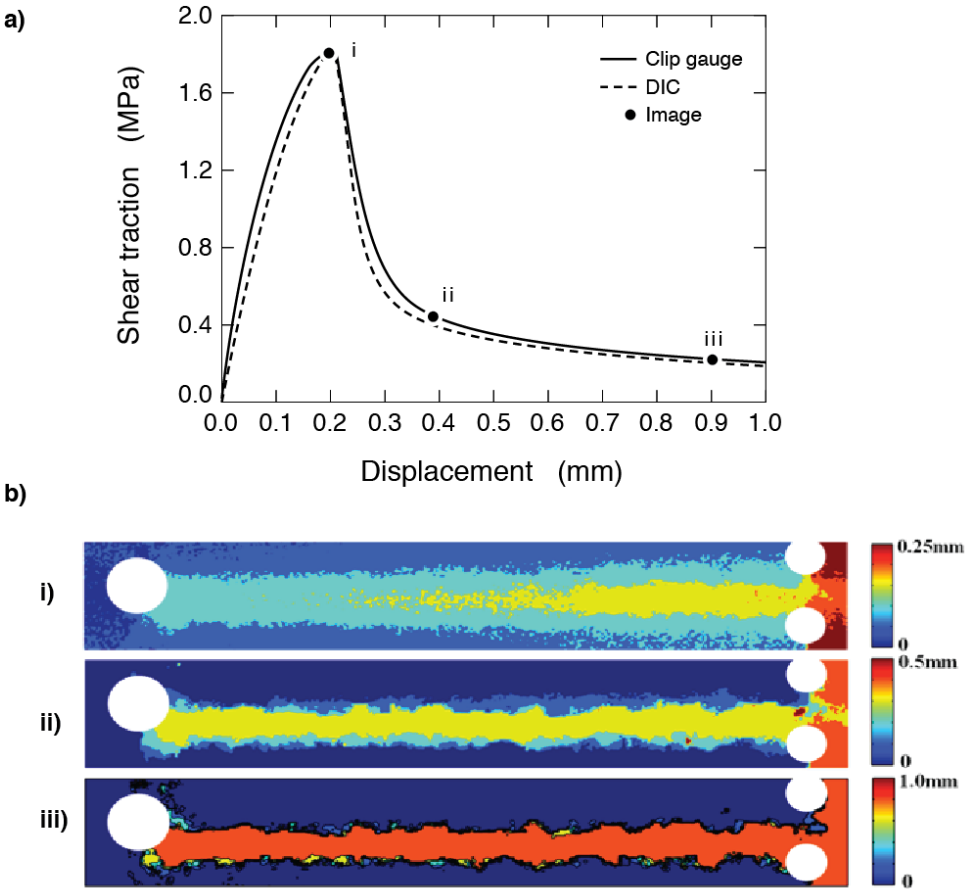

Fig. B4: Measured traction versus displacement relation from the double notch shear specimen. The displacement is measured via both a clip gauge and using digital image correlation (DIC). (b) Contours of displacement in *x*-direction on one side of the specimen (perpendicular to the shear planes).